Published by the American Institute of Aeronautics and Astronautics (AIAA) on 27 July 2024 for the AIAA Aviation Forum and ASCEND co-located Conference Proceedings. Published copies can be accessed via the AIAA Electronic Library via https://arc.aiaa.org/doi/10.2514/6.2024-4942 or https://doi.org/10.2514/6.2024-4942.

Development of a Plume Evolution Model for Launch Vehicle Ground Cloud Deposition

Nattanan Wongprapinkul*, Aaron W. Johnson†, Max Z. Li‡, Oliver Jia-Richards§, and Gokcin Cinar¶
University of Michigan, Ann Arbor, Michigan, USA

The study of rocket exhaust ground cloud evolution has been the focus of numerous research efforts. These studies aim to understand and predict the transport and dispersion of launch vehicle ground clouds under a variety of meteorological conditions, which consist of high concentrations of toxic acidic mixtures and particulate matters. Such understanding is critical for assessing environmental impacts and ensuring the safety of the areas surrounding the launch pad. However, the uncertainties increase with the involvement of atmospheric conditions. This study focuses on near-field and far-field acidic deposition, utilizing a Lagrangian Particle Dispersion Model (LPDM) as a principal model. Additionally, this study developed a separate cloud rise model with the objective of accurately predicting the vertical trajectories of rocket exhaust ground clouds, which are crucial for far-field deposition predictions. The near-field, far-field, and cloud rise models were validated using observed data from recent studies. Our results demonstrated good agreement when compared with the observed data. This model was integrated with the High-Resolution Rapid Refresh (HRRR) model to provide atmospheric data, enabling comprehensive simulations at any location and time in the US. The model extended its predictions to include the Starship integrated flight test launches at SpaceX Starbase launch pad in Boca Chica, Texas. The results, when combined with wind statistics, indicate a significant potential for the ground cloud to reach the residential areas. Although the propellant chosen for Starship is LOX/LCH$_4$, nitric oxide (NO) can be formed during the plume entrainment process, posing a risk to human health.

Nomenclature

$\mathbf{L}$	=	Particle initialization term, (m, m, m)
$\mathbf{r}_i$	=	Position vector of the i^{th} particle, (m, m, m)
t	=	Time, (s)
$\mathbf{V}$	=	Advection term, (m s^{-1})
$\mathbf{Z}$	=	Dispersion term, (m s^{-1})
$\mathbf{G}$	=	Settling term, (m s^{-1})
$\mathbf{B}$	=	Buoyancy term, (m s^{-1})
$\mathbf{E}$	=	Exhaust dynamics term, (m s^{-1})
w_t	=	Terminal settling velocity, (m s^{-1})
c_h	=	Dispersion velocity along horizontal axis, (m s^{-1})
c_v	=	Dispersion velocity along vertical axis, (m s^{-1})
K_h	=	Dispersion coefficient along horizontal axis, (m^2 s^{-1})
K_v	=	Dispersion coefficient along vertical axis, (m^2 s^{-1})
D	=	Particle diameter, (m)
ρ_s	=	Particle density, (kg m^{-3})
ρ_f	=	Fluid density, (kg m^{-3})

*Doctoral Student, Department of Aerospace Engineering, nattanan@umich.edu, AIAA Student Member.
†Assistant Professor, Department of Aerospace Engineering, aaronwj@umich.edu, AIAA Member
‡Assistant Professor, Department of Aerospace Engineering, Department of Civil and Environmental Engineering, Department of Industrial and Operations Engineering, maxzli@umich.edu, AIAA Member
§Assistant Professor, Department of Aerospace Engineering, oliverjr@umich.edu, AIAA Member.
¶Assistant Professor, Department of Aerospace Engineering, cinar@umich.edu, AIAA Senior Member.

μ = Dynamic viscosity, (kg m^{-1} s^{-1})
F_d = Drag force acts on particle, (kg m s^{-2})
v = Particle velocity, (m s^{-1})
x = Downwind distance, (m)
$z(x)$ = Height of the plume center at x, (m)
β = Entrainment constant
F_b = Buoyancy flux, (m^4 s^{-3})
u = Mean wind speed, (m s^{-1})
g = Acceleration of gravity, (m s^{-2})
w_0 = Plume initial vertical velocity, (m s^{-1})
r = Plume initial radius, (m)
T_a = Ambient temperature, (K)
T_f = Plume temperature, (K)
s = Atmospheric stability parameter, (s^{-2})
θ = Potential temperature, (K)
w_b = Plume rise rate, (m s^{-1})
P = Plume absolute pressure, (kg $m^{-1}s^{-2}$)
V = Plume volume, (m^3)
R = Specific gas constant, (J K^{-1} mol^{-1})
$\bar{R}$ = Plume specific gas constant, (J K^{-1} mol^{-1})
γ = Specific heat ratio
M_a = Amount of entrained air in the plume, (kg)
M_e = Amount of burned propellant in the plume, (kg)

I. Introduction

The growing space economy and increased rocket launches emphasize the need for comprehensive research and assessment to understand and mitigate the environmental impact of space missions. The environmental consequences of rocket launches encompass two distinct dimensions. Firstly, changes in the local environment occur due to the acidic deposition resulting from the rainout of ground clouds, which form and are transported by the wind. Secondly, the widespread dispersion of exhaust emissions at higher altitudes can potentially impact the global environment [1]. This study primarily focuses on the local environmental impacts of the Space Shuttle launches, with a particular emphasis on the exhaust from the solid rocket motors (SRMs), which contains aluminum particles, chloride compounds such as hydrochloric acid (HCl), and elements including hydrogen, nitrogen, carbon, and oxygen [2]. The Space Shuttle launches, which were frequent events, have been extensively studied for their environmental impacts. Across the program, a total of 135 launches took place. The effects of the acid ground clouds on the environment following each launch have been both observed and documented [3]. The substantial quantities of acid rain and aluminum particles from the ground cloud have significant effects on soil, water quality, and biota. The area of acute impacts led to alterations in vegetation and the deaths of small fish in shallow waters near the launch pad [3, 4].

This study developed a ground cloud rocket evolution model aimed at predicting acid deposition resulting from the SRMs. The model's outcomes include deposition area, distance, and contour/outline, enabling us to assess and identify patterns and regions that are typically susceptible to acidic deposition. The exhaust cloud deposition occurrence has been categorized into two launch cloud deposition characteristics: near-field and far-field deposition [5]. According to the launches of the Space Shuttle program at launch pads 39A and 39B at the Kennedy Space Center (KSC), the SRM exhaust was directed to the north by the flame trench. When the two SRMs were ignited, they produced acidic mixtures as the exhaust vaporized and coalesced with the deluge water [3], which is the water-based acoustic suppression systems typically activated 12 seconds before the Space Shuttle launch. The deluge water may have a significant effect on the behavior of the ground cloud rise [6]. The rapid deposition of acidic mixtures in the vicinity of the launch pad is known as near-field deposition. Previous studies have indicated that near-field deposition range typically falls within 0.5 to 1.6 kilometers from the launch pad[3, 7]. Far-field deposition occurs when certain small acidic mixtures within the ground cloud are transported by prevailing winds [3]. Simultaneously, as the ground cloud ascends, the process of acidic rainout becomes evident. The cloud continues to rise until it reaches the cloud stabilization height and drifts with the wind. Acidic mixtures that fall out from this ground cloud to the ground result in what is known as far-field deposition [8].

A study on the exhaust cloud measurements was conducted by Turner in 1983 [9], including a series of photographs that captured the development of the cloud over time for the STS-1, STS-2, STS-3, and STS-4 launches. The exhaust plume ascends to a height where it becomes buoyantly stable with the surrounding air, reaching this balance between 1 and 2 km above ground within 5 to 10 minutes after the takeoff. Once stabilized, the movement of the exhaust begins to be primarily driven by the surrounding atmospheric conditions. By the time it reaches equilibrium, the exhaust cloud typically has about 99 percent of the entrained air [9]. An in-depth investigation of the substances present in the cloud was carried out by Gregory in 1981 [10]. During the STS-1 launch, a Cessna 402 aircraft was deployed to collect data on hydrogen chloride (HCl), particulate matter, temperature, and dew point. The aircraft flew through the cloud's centroid area, guided by assistance from the ground.

Prior studies help guide and provide a better understanding of ground cloud behavior, while experimental data helps fine-tune the model to enhance accuracy. The Rocket Exhaust Effluence Dispersion Model (REEDM) is widely employed for predicting launch cloud deposition [11]. The REEDM shows qualitative agreement with ground observations regarding deposition and the direction of the cloud path. However, it tends to overestimate both the total deposition area and the maximum distance at which deposition is observed from the launch pad. The REEDM was developed to predict rocket exhaust effluent concentrations, enabling the prediction of far-field deposition resulting from the acid rainout from the ascent ground cloud. One inherent limitation of the REEDM lies in its inability to predict near-field deposition [8]. Despite the area of near-field deposition being relatively small, its high concentration of the acidic mixtures deposition makes it crucial. Far-field deposition typically exhibits minimal impacts, often limited to periodic spotting on plant leaves. There has been no observed plant mortality, nor have there been any noticeable alterations in the composition or structure of the plant communities in the far field [12]. In contrast, near-field deposition exerts a significant influence on the immediate surroundings, leading to issues such as small fish kills, damage to vegetation, and alterations in soil surface chemistry [12, 13]. Vegetation damage correlated with chloride deposition levels, with significant damage to various species at levels over 1,000 mg/m^2 and sensitive species affected at 100 mg/m^2 or less [8]. Furthermore, under severe meteorological conditions, high wind magnitudes can expand the near-field deposition area, further extending the range of severe impacts to cover a larger area.

The Lagrangian particle dispersion model (LPDM) is widely used to simulate particle transport in the atmosphere and can be adapted for specific problems, such as by adding a buoyancy model to simulate the transportation of hot plumes from sources such as volcanoes, rockets, or industrial activities. Additionally, it can be used to study particle transport in turbulent flow by incorporating stochastic models that account for the effects of turbulence. In this context, the accuracy of the model relies heavily on the fidelity of the stochastic model. Moreover, the representation of relevant physical phenomena must strike a balance between achieving accuracy and managing computational costs [14]. This study presents a LPDM to comprehensively simulate and predict both near- and far-field deposition under various meteorological conditions. This study also developed a cloud rise model based on the "2/3 law", an empirical model that has been tested through field experiments and laboratory tests proposed by Briggs [15]. The cloud rise model enhances the adaptability of the main model and enables it to predict cloud rise under various meteorological conditions, which is crucial and sensitive for far-field deposition results.

II. Lagrangian Particle Dispersion Model (LPDM)

In this study, a LPDM was developed with the goal of predicting near- and far-field deposition from a rocket launch. From the prior studies, this model was employed to simulate volcanic ash dispersion, which can predict ash fallout. The model predictions align well with the reported data, particularly when conducted in accordance with the real-time volcanic emission rate [16]. The model in this study was specifically developed to simulate trajectories in three-dimensional space for acidic mixtures emitted from the SRMs, aiming to predict deposition. This model incorporates five main mechanisms: advection, dispersion, settling [17], buoyancy, and exhaust dynamics. Given a collection of n particles, the discretized governing equation for the position of particle i is

$$r_i(t + \Delta t) = r_i(t) + \mathbf{V}\Delta t + \mathbf{Z}\Delta t + \mathbf{G}\Delta t + \mathbf{B}\Delta t + \mathbf{E}\Delta t; \quad r_i(0) = \mathbf{L}, \tag{1}$$

where $\mathbf{L}$ is the particle initial position, $\mathbf{V}$ represents advection with the local wind, $\mathbf{Z}$ represents dispersion, $\mathbf{G}$ represents settling due to gravitational forces, $\mathbf{B}$ represents buoyancy, and $\mathbf{E}$ represents the initial particle velocity minus the change in velocity caused by atmospheric drag. In the initial step, particles were ejected from a point source in a northern direction, simulating the release of hydrochloric acid and aluminum particles from the SRMs, which coagulated with the deluge water. The new position vectors will be calculated using the previous solution, along with the application of the four main mechanisms mentioned above to individual particles.

The advection term relies on a four-dimensional wind dataset that includes level, time, latitude, and longitude. This advection assumption presumes particle transportation in alignment with the wind, disregarding drag [17]. Wind transport calculations involve the utilization of trilinear interpolation with the four-dimensional wind dataset to obtain the wind data at the location of each particle. Particle dispersion represents the behavior of particles spreading in the atmosphere. To simulate the unpredictable movement of particles, the dispersion velocity, **Z**, is introduced as a stochastic element, calculated using Gaussian random numbers. **Z** consists of two components, c_h and c_v, denoting dispersion along horizontal and vertical axes. In three-dimensional space, c_h controls diffusion along the Earth's surface (x and y axes), while c_v controls diffusion in the vertical direction (z axis, representing altitude). The rate of diffusion is individually applied to each particle and calculated using

$$c_h = \sqrt{2K_h/\Delta t}, \qquad \text{and} \qquad c_v = \sqrt{2K_v/\Delta t}. \tag{2}$$

Here, K_h and K_v represent the horizontal and vertical dispersion coefficients, respectively. The model assigns values of 1 m^2/s to both K_h and K_v for a normal launch condition [18].

The gravitational settling term, denoted as **G**, determines the terminal velocity of particles based on their density and diameter, and is calculated using Stoke's law

$$\|\mathbf{G}\| = \frac{2}{9}\frac{(\rho_s - \rho_f)gD^2}{4\mu}, \tag{3}$$

where ρ_s and ρ_f are the particle and fluid densities, g is the local gravitational acceleration, D is the particle diameter, and μ is the dynamic viscosity. The direction of the gravitational settling velocity is towards the ground. In the model, after particles are emitted from the point source into the atmosphere, they experience a deceleration process due to drag, gradually reducing their speed over time. Stoke's law is employed to calculate the drag force

$$F_d = 3\pi D\mu v. \tag{4}$$

By combining the drag force with the mass of the particle and assuming constant acceleration throughout the time interval, one can use the equations of motion to derive the change in velocity due to atmospheric drag, which is then applied to **E**.

The near-field deposition particle size distribution was determined based on the total aluminum analysis of the near-field exhaust deposition collected during STS-11, as reported in the previous study [2]. This data has been selected for its comprehensive analysis of the particle size distribution. For far-field deposition particle size distribution, while the prior study did not specify a particular particle size, it has been noted that the particle size is relatively small compared to that of the near-field [3]. In this study, we assume a far-field deposition particle size distribution with a mean particle size of 63 μm and a standard deviation of 10^{-6}. The particle size distributions are illustrated in Figure 1. The far-field deposition occurs due to the acidic fallout from the ground cloud that rose and stabilized. One crucial factor influencing the deposition pattern is the characteristics and behavior of the ground cloud's ascent which was described in the following section.

III. Cloud Rise Model

In this section, cloud rise theories for hot buoyant plume were explained. This study utilized the "2/3 law" to describe the plume rise for bent-over buoyant plumes. For neutral conditions and the transitional phase, the plume rise equation that defines the cloud altitude, z, is given by

$$z(x) = \left(\frac{3}{2\beta^2}\right)^{1/3} F_b^{1/3} x^{2/3} u^{-1}, \tag{5}$$

where β is the entrainment constant, x is the downwind distance, and u is the mean wind speed. F_b is the buoyancy flux

$$F_b = g w_0 r^2 (T_f - T_a)/T_f, \tag{6}$$

where w_0 is the plume initial vertical velocity, r is the plume initial radius, and T_f and T_a are the plume and ambient temperature. For stable conditions and final phase, the final plume height is given by

$$z = 2.6\left(\frac{F_b}{us}\right)^{1/3}, \tag{7}$$

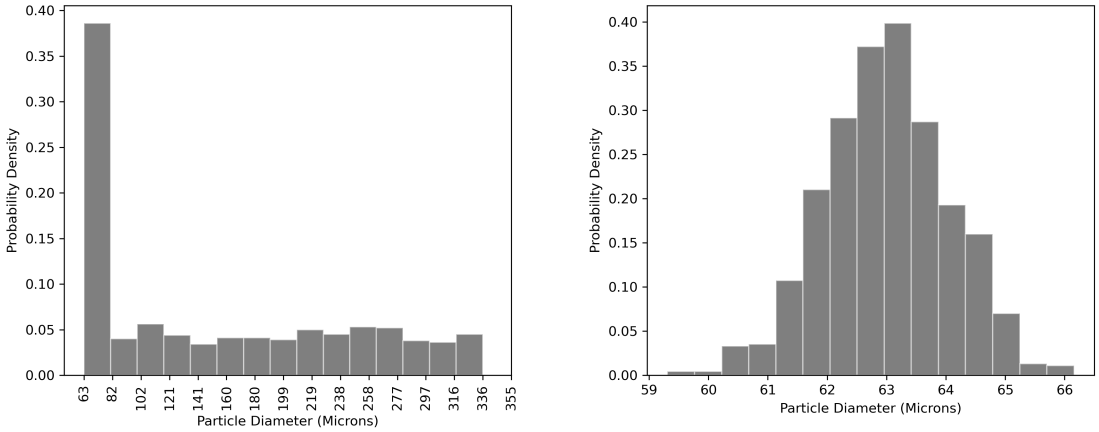

Fig. 1 Particle diameter distributions for near-field deposition (left) and far-field deposition (right).

where s is the atmospheric stability parameter dependent on the potential temperature, θ,

$$s = \frac{g}{\theta}\frac{\partial \theta}{\partial z}. \tag{8}$$

This formula has been widely used for particle models and is supported by experiments and field observations [15].

Anfossi [19, 20] showed the possibility of generalizing equation 5 and 7 that developed based on different phase and atmospheric conditions to a single expression. It can be rewritten as:

$$z(x) = 2.6\left(\frac{F_b^{1/3}}{u}\right)x^{2/3}\left(\frac{x^2 s}{u^2} + 4.3\right)^{-1/3}. \tag{9}$$

The final expression can be written as a function of time

$$z(t) = 2.6\left(\frac{F_b t^2}{u}\right)^{1/3}\left(t^2 s + 4.3\right)^{-1/3}. \tag{10}$$

The buoyancy mechanism is driven by utilizing 10 to compute the rise rate, w_b, by

$$w_b = \Delta z/\Delta t = [z(u, s, t + \Delta t) - z(u, s, t)]/\Delta t. \tag{11}$$

In order to calculate the initial plume radius, r, used in Equation 6, the ideal gas law was implemented as shown in Equation 12 to calculate the plume volume [21]. Assuming the plume has a spherical shape, the radius of the plume can be calculated from the plume volume, V based on

$$PV = \frac{(M_a + M_e)\bar{R}T_a}{1 - \frac{\gamma-1}{\gamma}\frac{E_{in}}{PV} + \frac{M_e R T_a}{PV}}, \tag{12}$$

where P is the plume absolute pressure, M_a and M_e are the amount of entrained air and burned propellant in the plume, $\bar{R}$ is the plume specific gas constant, γ is the specific heat ratio, and E_{in} is the overall energy input.

The ground cloud is composed of the exhaust products from 10 seconds of boosters firing. It was also mentioned that the mass flow rate of the propellant for the two SRBs on the Titan III C for the first 10 seconds of firing is approximately 4,536 kg/s [21]. This study extends findings to estimate the M_e in the ground cloud for the UA1207 booster used in the Space Shuttle program. Based on the sizing data between the two boosters [22], which share the same diameter, and taking into account the propellant weight, it is assumed that the increase in burn rate is linear. Thus, two UA1207 boosters are estimated to have a propellant flow rate of about 6,055 kg/s, resulting in an estimated ground cloud M_e of 60,550 kg over 10 seconds of firing. It was also mentioned by Hart (1972) [21] that the amount of entrained air, M_a, is around 256 times the original amount of the propellant burned inside the control volume, M_e.

Table 1 Summary of case-specific optimization results with Coefficient of Determination (R^2), and Root Mean Square Error (RMSE).

Case	w_0 (m/s)	R^2	RMSE (m)
STS-1	2.16	0.88	104.3
STS-2	3.71	0.90	98.9
STS-3	0.10	0.83	95.2
AP-14	4.48	0.98	59.3
AP-15	3.45	0.95	115.7
AP-16	3.71	0.96	88.1

To calculate the specific gas constant, $\bar{R}$, for the rocket exhaust gas and air mixture within a control volume, one must ascertain the average molar mass of the exhaust gas mixture. For the exhaust composition of the Space Shuttle's SRBs as reported in the referenced study [23], the average molar mass can be calculated to be approximately 20.253 g/mol. Given M_e and M_a, the overall specific gas constant, $\bar{R}$, for the control volume is calculated by taking a mass-weighted average, resulting in approximately 287.5 J/(kg·K). The resulting $\bar{R}$ closely approximates the specific gas constant of air, due to the substantially greater mass of air in the control volume compared to the mass of the exhaust gases.

The overall energy input, E_{in}, can be calculated using the specific energy, which equals 6,629,100 J/kg [21], multiplied by M_e. The conservation of energy within the control volume was used to calculate the final cloud temperature at lift-off, denoted as T_f,

$$T_f = \frac{T_a}{1 - \frac{\gamma-1}{\gamma}\frac{E_{in}}{PV} + \frac{M_e R T_a}{PV}}. \tag{13}$$

As previously noted, accurately characterizing cloud rise is a critical component for far-field deposition modeling. The importance of this factor is amplified when encountering abrupt shifts in wind characteristics at different altitudes. Such variations increase the sensitivity of the far-field model to the cloud rise. Consequently, it is essential to provide a well-defined and precise representation of cloud rise behavior to ensure the robustness of the deposition predictions.

IV. Results

A. Cloud Rise

The cloud rise model was validated with the observation cases to ensure its accuracy and reliability. Field data from observed cloud rise events were compared with the predicted results to determine any discrepancies and to fine-tune the model parameters as in this cases it is the plume initial vertical velocity, w_0. This process helped to ensure that the model can be confidently applied to predict cloud rise behavior in a variety of meteorological conditions.

The optimization process considered both the Root Mean Square Error (RMSE) and the Coefficient of Determination (R^2) to evaluate model performance. This process utilized the grid search method by varying w_0 to find the value that minimizes the data error. We can observe that equation 10 exhibits monotonic behavior with respect to w_0. It either strictly increases or decreases. Therefore, the data error possesses a single extremum within the feasible range of w_0, which serves as both the local and global minimum of the function. The range of w_0 to perform model fitting is 0.10 m/s to 5.00 m/s with the step size of 0.01 m/s. Six observation cases were used to validate the model, consisting of STS-1, 2, and 3 from Anderson, 1983 [24] , as well as Apollo 14, 15, and 16 cloud rise data from Susko, 1968 [25]. For the three Apollo cases, the values of M_e and E_{in} differed from those in the Space Shuttle cases. The specific values were retrieved and calculated using the data from Susko, 1968, Susko, 1973, Stephens, 1973, and Gregory, 1974 [25–28]. Furthermore, for Apollo cases, the temporal data were collected by measuring the top cloud, as opposed to recording the centroid position [26]. This study implemented case-specific optimization to analyse the trend of w_0 as shown in Table 1. Table 1 shows that the value of w_0 minimizing the error for each case lies between 0.10 m/s and 4.48 m/s. However, an outlier value of 0.10 m/s is observed for the STS-3 case.

Excluding the STS-3 case from the model's optimization results in a value of w_0 of 3.50 m/s; the evaluation is presented in Table 2. Figures 2 and 3 present the predicted and observed center cloud rise data for each case. The

Table 2 Optimization results highlighting the optimal initial cloud vertical velocity (w_0) of 3.5 m/s, with corresponding Coefficient of Determination (R^2), and Root Mean Square Error (RMSE) for each case.

Case	R^2	RMSE (m)
STS-1	0.83	124.4
STS-2	0.89	100.5
STS-3	-3.18	479.1
AP-14	0.94	90.7
AP-15	0.95	115.8
AP-16	0.96	90.6

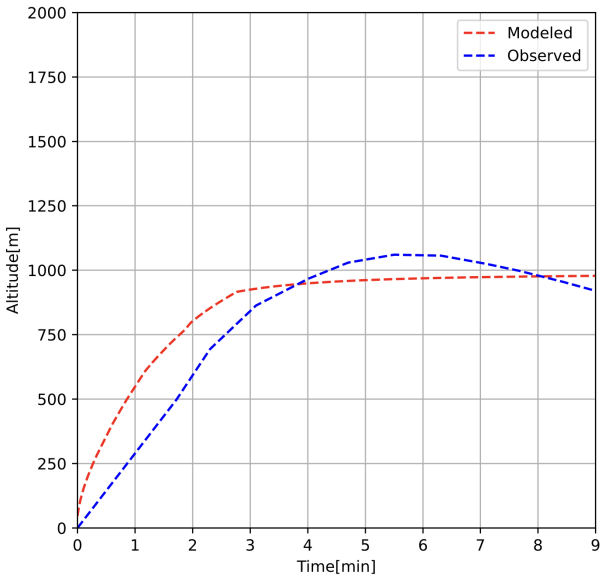

(a) STS-1.

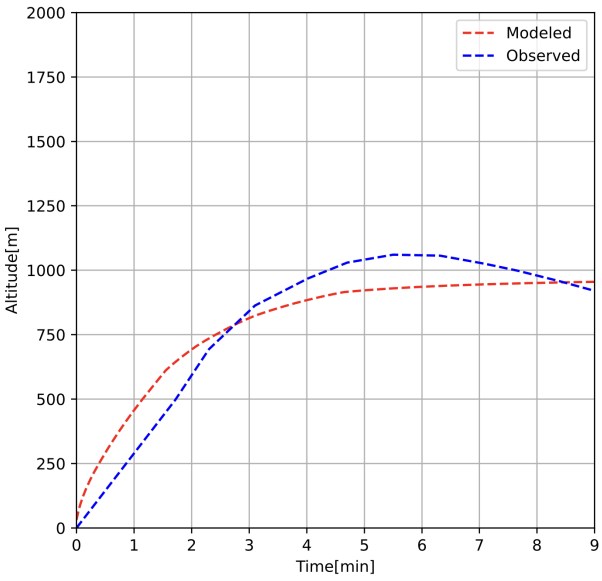

(b) STS-2.

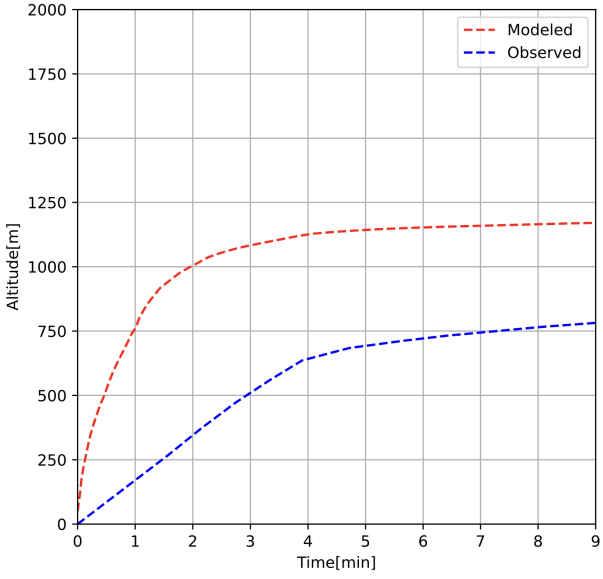

(c) STS-3.

Fig. 2 Predicted and observed center cloud rise data for STS-1, 2, and 3.

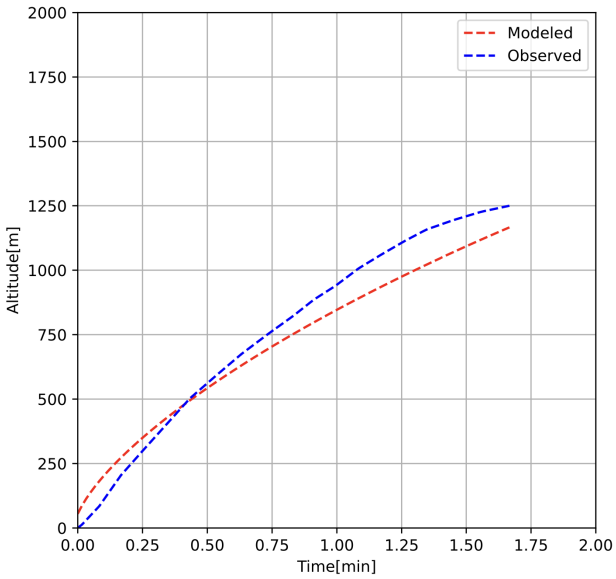

(a) Apollo 14.

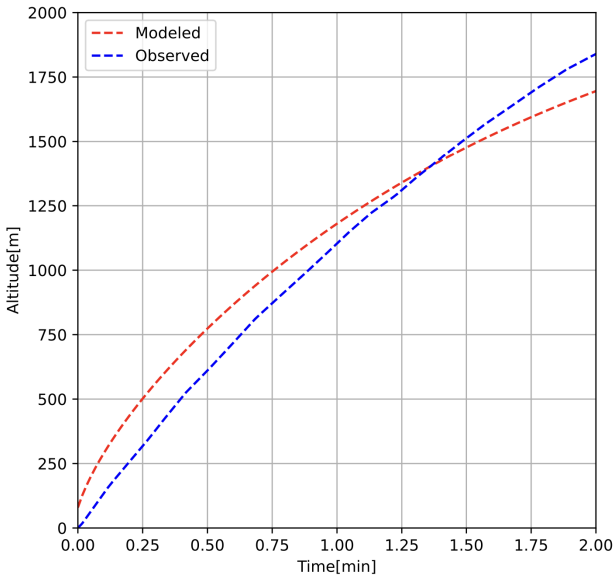

(b) Apollo 15.

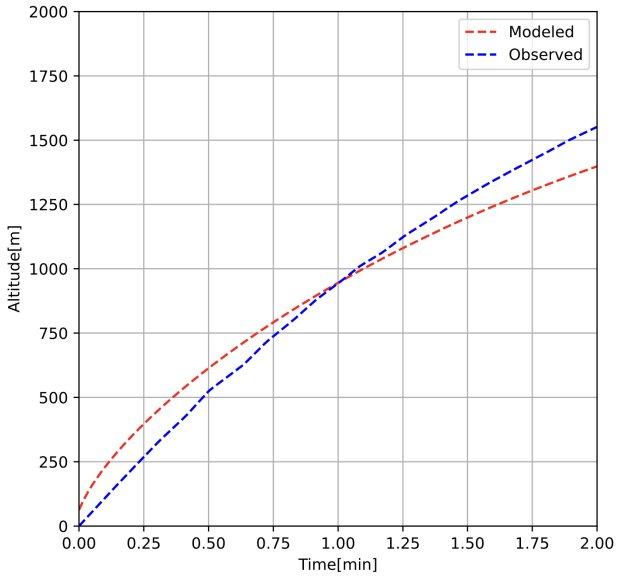

(c) Apollo 16.

Fig. 3 Predicted and observed center cloud rise data for Apollo 14, 15, and 16.

plots clearly demonstrate that the predicted data are in good agreement with the observed data. However, the model overpredicts the cloud rise data for the STS-3 case. The observed altitude of the cloud's center for the STS-3 case at 9 mins is around 750 m, compared to about 1,200 m predicted by the model. Upon observing the atmospheric conditions and comparing the STS-1, STS-2, and STS-3 cases, we find that the stability parameter for the STS-3 case follows that of the STS-2 case. However, the wind speed shows the lowest magnitude at altitudes below 1,000 m. Equations 9 and 10 explain that a relatively low wind magnitude leads to a higher rise rate, resulting in greater cloud height, which is why the model predicted a higher cloud altitude for STS-3 than for STS-1 and STS-2. When incorporating atmospheric variables into the model, it is crucial to acknowledge and understand the associated uncertainties. Despite these uncertainties, the data we currently possess indicate that the model generally provides a good agreement with the observed data. However, there might be instances where the agreement is not as strong, reflecting the inherent complexity of modeling atmospheric phenomena.

B. Deposition Characteristics

Cumulative near-field deposition data from STS-1 through STS-9 cases were simulated and depicted in Figure 4. To enhance visual clarity and facilitate frequency evaluation, the shaded area representing near-field deposition has been included. As a reference, the blue dashed line indicates the edge of launch pad 39A at Cape Canaveral. In the near-field deposition model, the key parameter input is the wind speed and direction at 1 minute average prior to launch time. Detailed information regarding the deposition area, distance, and wind condition for each launch is provided in Table 3. The deposition area ranges from 0.11 to 0.20 km^2, with the farthest distance from the launch pad ranging between 428 and 744 m. The primary factor influencing the overall pattern is the wind profile specific to each STS launch. From the model's result, STS-5 case exhibits the greatest deposition area of 0.20 km^2 due to a strong wind speed of 6.7 m/s from the east (90°N). The wind traveled across the initial exhaust plume from the SRMs, which was directed northward, resulting in significant shear and the dispersion of particles over a wide area.

Dreschel, 1990 and Schmalzer, 1992 [3, 7] mentioned that the area impacted fluctuates based on the wind conditions during liftoff, typically spanning approximately 0.5 to 1.6 km from the launch pad. In the model, the farthest deposition distance, observed to be 744 m, occurred during the STS-9 launch, a result of the supportive winds that aligned with the northward direction of the initial exhaust plume. The illustrations from Schmalzer, 1985 and Schmalzer, 1993 [7, 13] were used in the near-field validation process, mainly compare with the deposition patterns. The comparisons show a good agreement with respect to the deposition frequency and fundamental behaviors of deposition. Substantial portions of the near-field deposition from STS-8 and STS-9 extended into the Atlantic Ocean, a pattern that is also evident in the observed data.

Table 3 Wind conditions and near-field launch deposition results for STS-1 through STS-9.

Case	Wind speed (m/s)	Wind direction (°N)	Area (km^2)	Distance (m)
STS-1	3.6	125	0.14	564
STS-2	8.2	345	0.17	446
STS-3	2.1	50	0.13	482
STS-4	1.8	133	0.11	517
STS-5	6.7	90	0.20	659
STS-6	3.9	63	0.13	452
STS-7	1.8	10	0.12	428
STS-8	2.7	269	0.14	509
STS-9	5.8	183	0.15	744

For the far-field deposition model, we used the same cases as those in the near-field deposition simulation. Figure 5 displays the simulated cumulative far-field deposition from STS-1 through STS-9. The key parameter in the far-field deposition model is the wind data for STS-1 through STS-9 at the time of launch, ranging from sea level to 5,000 ft. [29–33]. Observed data were obtained from Duncan, 1994 [5]. These data include deposition areas and distances for each launch, determined through GIS analysis. The deposition patterns illustrated by Schmalzer, 1986 [8] were utilized for a comparative analysis with the characteristics of the predicted deposition results. Copper plates served as collection

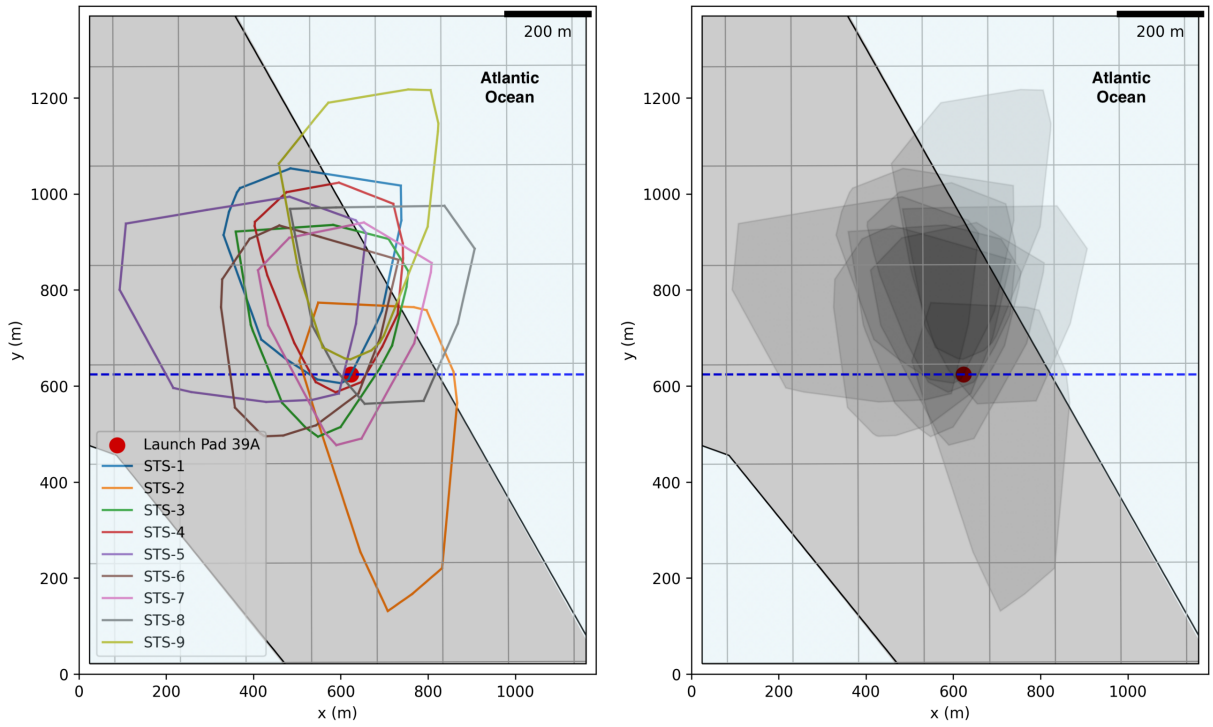

Fig. 4 Cumulative near-field launch deposition results for STS-1 through STS-9.

instruments for observing deposits during several early launch events, which presented challenges in comprehensively determining the far-field deposition characteristics [8]. The accuracy of the observed far-field deposition characteristics is heavily dependent on both the location and abundance of the copper plates. Table 4 presents comparisons between the observed data and the modeled results for far-field deposition area and distance.

For STS-1 and STS-6, exhibiting similar wind speeds and directions, the predicted results indicate that deposition occurred to the northwest of Launch Pad 39A. Owing to a higher standard deviation in wind direction for STS-6, a larger area of deposition extending from west to northeast of the launch pad was observed. The patterns of deposition agree well with the observed data. The predicted deposition distances for STS-1 and STS-6 are similar. However, the model overpredicted the ground data in terms of both area and distance. With an average wind magnitude of 3.14 m/s, STS-7 experienced the weakest winds. Consequently, the model predicted both the smallest deposition area and the shortest distance of all the scenarios. Nevertheless, it underpredicted the actual observations.

Both the observed data and the predicted results indicate that the STS-2 launch resulted in a relatively large deposition area and distance, due to a strong wind magnitude combined with a significant standard deviation in wind direction. The deposition pattern corresponds well with the observed map, showing deposition occurring to the south of the launch pad, along the Banana River, and in parts of the land. The predicted deposition area and distance are similar to the observed data, with a slight overprediction in the deposition area. STS-5 had a similar wind magnitude to STS-2, but the direction pointed west of the launch pad instead. With a slightly higher wind magnitude, the model predicted a longer deposition distance. One can observe a low standard deviation, leading to smaller deposition area compared to STS-2 case. The model overpredicted both the deposition area and distance. The deposition map from Schmalzer, 1986 shows that deposition occurred to the west of the launch pad, crossing the Indian River in a manner similar to what is displayed in Figure 5. However, when compared to the scale, this does not correspond with the GIS analysis from Duncan, 1994 which indicates a deposition distance of only 11.76 km. The results did not include the cases of STS-3, 4, 8, and 9, as the launch cloud primarily moved over the Atlantic Ocean soon after launch. This made it difficult to determine the ground deposition pattern.

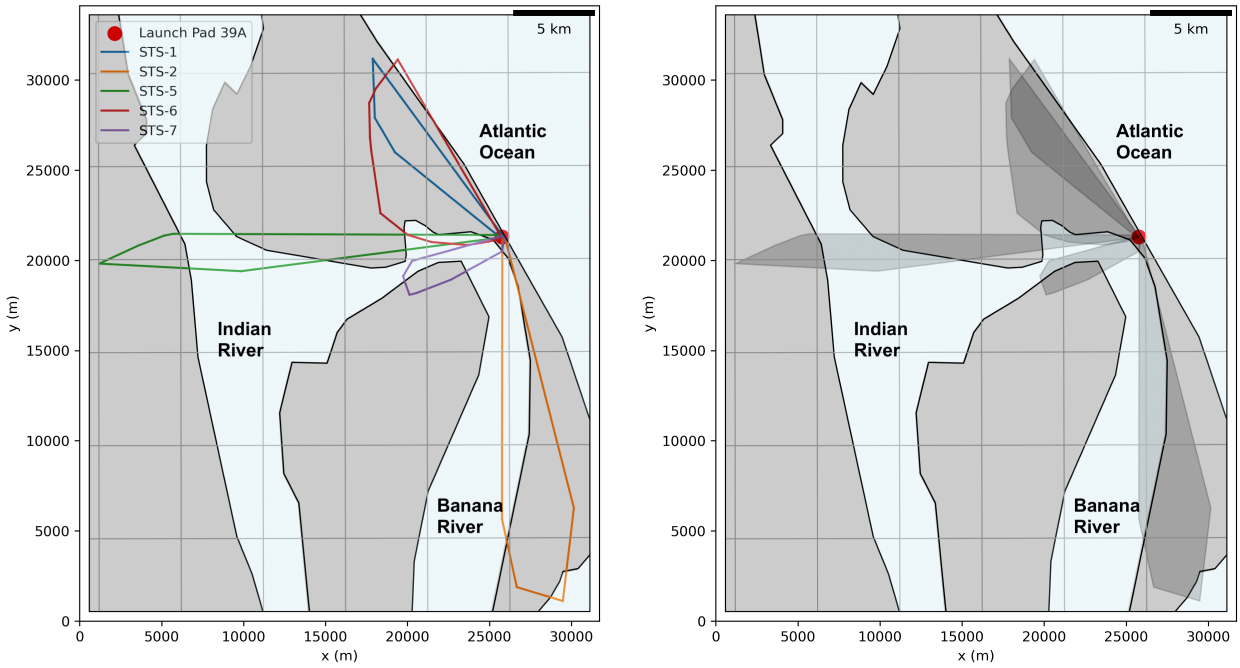

Fig. 5 Cumulative far-field launch deposition results for STS-1 through STS-9.

Table 4 Wind conditions and far-field launch deposition results for STS-1 through STS-9.

Launch cases	Avg. wind speed (m/s)	Wind direction (°N)		Deposition area (km^2)		Deposition distance (km)	
		Avg.	SD	Observed	Predicted	Observed	Predicted
STS-1	5.52	126.04	32.03	7.30	17.23	7.87	13.18
STS-2	9.26	7.71	16.19	46.59	53.99	21.85	21.90
STS-5	10.41	83.57	6.41	18.40	31.58	11.76	24.05
STS-6	5.50	155.84	51.31	6.49	46.36	4.83	12.32
STS-7	3.14	62.43	19.51	12.83	9.13	9.71	6.46

C. Deposition Concentration

To validate the model with respect to concentration, several challenges arise due to real-world uncertainties, such as variable wind velocities and directions, turbulent flow, chemical reactions, and droplet formation resulting from the interaction between exhaust emissions and deluge water. This phase of model validation is designed to confirm the model's ability to accurately capture the critical trends and patterns of plume evolution and consequential deposition concentrations.

For the near-field deposition model, a comparison was conducted between observed data from Drechsel, 1990 [3] and the model's predicted concentrations. The observed data, provided in 3-D plots, present a challenge for extracting precise values; thus, making a comprehensive comparison with the model results during the validation process difficult. This observed data included measurements of hydrochloric acid and particulate deposition taken during the launches of STS-11, STS-13, and STS-14. The examined study area, situated 400 m north of launch pad 39A, spanned 420 $\times$ 300 m. The observational data provided 3-D plots of the acidic deposition, which consisted of particulate and chloride deposition. However, the observational data show a high correlation between particulates and chlorides, with Pearson product-moment correlation coefficients of 0.93 for STS-14 and 0.70 for STS-11 and STS-13. As a result, this section focuses on validating chloride deposition, and, due to the high correlation factor, it also allows for an accurate approximation of particulate deposition.

We examined the peaks and trends illustrated in the 3D representation of data from Dreschel's study [3]. In the case

Table 5 Summary of near-field acidic deposition concentration results for STS-11, 13, and 14.

Launch cases	Wind speed (m/s)	Wind direction (degree north)	Peak deposition (g/m^2)		Peak deposition location (y-axis) (m)	
			Observed	Predicted	Observed	Predicted
STS-11	1.1	180	90	98	250	200
STS-13	5	300	50	80	375	250
STS-14	0.9	180	110	103	300	200

of STS-11, the wind was from the south (180°N) at 1.1 m/s. The 3D graph in Drechsel, 1990 depicts a distinct peak at the 0 m mark on the x-axis 250 m mark on the y-axis, indicating the highest chloride concentration of approximately 90 g/m^2. The deposition concentration gradually decreases along the x-axis, with values approximately 60 g/m^2 at the center of the graph and about 25 g/m^2 at the end of the x-axis. Similarly, form Figure 6 (a), our model exhibits a peak at the beginning of the x-axis, showing a concentration of 98 g/m^2, which is slightly higher than the observed data. A similar trend can be observed, with density decreasing along the x-axis; the deposition concentration is approximately 10 g/m^2 at the end of the x-axis.

For the STS-13 case, the wind was from the north (300°N) at 5.0 m/s. The observed data show that deposition influenced by the moderate wind prevailing against the plume's direction. The peak concentration with the concentration around 50 g/m^2 was located at the 0 m mark on the x-axis and at the 375 m mark on the y-axis. Compare to model's result as shown in Figure 6 (b). It indicates that the overall deposition trend differs from that observed in the STS-11 case, primarily due to changes in wind direction and magnitude. The maximum concentration of around 80 g/m^2 can be observed at 250 m mark on the y-axis. The overall behavior and areas of deposition display a reasonable agreement when compared with the observed data.

The STS-14 case exhibited a wind profile similar to that of STS-11, with wind coming from the south (180 ° N) at 0.9 m/s. For the observed data, under these conditions, one might expect the deposition profile to be nearly identical to the STS-11 case. However, a distinct pattern can be observed. The peak concentration, as anticipated, occurred at the beginning of the x-axis, with a density of 110 g/m^2. The deposition was slightly lower along the y-axis; however, it increased to approximately 100 g/m^2 at 150 m on the x-axis. Another principal difference is the location of the approximate center of deposition, which is around 300 m on the y-axis. Given the meteorological conditions, one would not expect the center of deposition to shift to 300 m, considering that the midpoint is 200 m. This reflects the inherent uncontrollable uncertainties. Compared to the predicted results from the model, as shown in Figure 6 (c), the plot is nearly identical to that of the STS-11 predicted results, with the peak at the same location and a magnitude of approximately 103 g/m^2. Overall, it exhibits a trend similar to the STS-11 case as a result of comparable wind conditions. Table 5 summarizes the acidic deposition trends from observed data and predicted data for STS-11, 13, and 14.

Validating far-field deposition concentrations presents significant challenges due to the scarcity of available data and inconsistencies in the methods used to collect observed data. Given these constraints, a detailed comparison is not feasible. Instead, an order of magnitude comparison is conducted as it provides a broad assessment of the model's predictive capabilities. This allows for the evaluation of whether the model captures the general scale of deposition despite the absence of precise data. Such an analysis can still offer valuable insights into the model's reliability and can guide further refinement. Similarly to the near-field analysis, this section focuses on validating chloride deposition since the availability of more extensive observed data, in contrast to aluminum oxide, and the environmental impacts for far-field are more specifically associated with chloride deposition.

STS-51D and STS-51B are two launch cases that were used to validate acidic deposition concentrations for a far-field deposition model. The observed data used for validation were obtained from Schmalzer, 1986 [8]. Data was collected by gathering leaf samples from the deposition path, which were then washed to recover deposited materials. For STS-51D, there were three useful sample sites: D-1, D-2, and D-4. The D-4 site was situated approximately 600 m north of launch pad 39A, measured from the northern edge of the launch pad, and lay just beyond the border of the near-field damage described in the paper. Concentrations of approximately 2,215 and 1,622 mg/m^2 were observed at the D-4 site. Figure 7 displays the results of far-field deposition for the STS-51D case. The model predicts a maximum acidic deposition concentration of 1,967 mg/m^2 at around the left of the launch pad. The D-2 site, situated approximately 1.8 km downwind of the launch pad, recorded concentrations of approximately 44 and 26 mg/m^2. Meanwhile, the D-1 site, located nearly 7 km away, noted a concentration of about 67 mg/m^2. Figure 8 excludes deposition concentrations lower than 100 mg/m^2 to facilitate visualization. It can be observed that high concentrations of deposition, exceeding 100

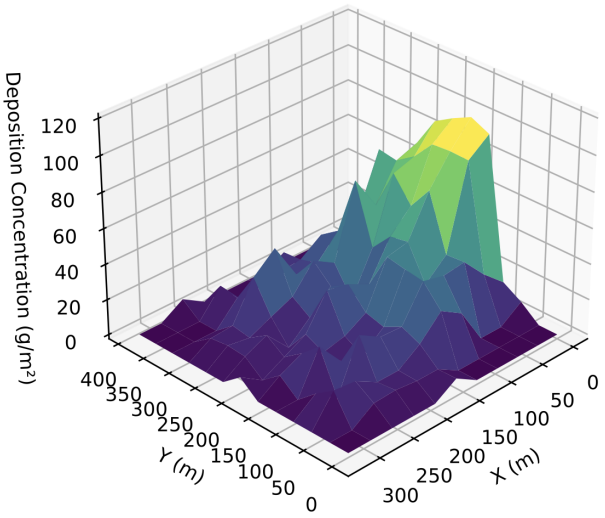

(a) STS-11.

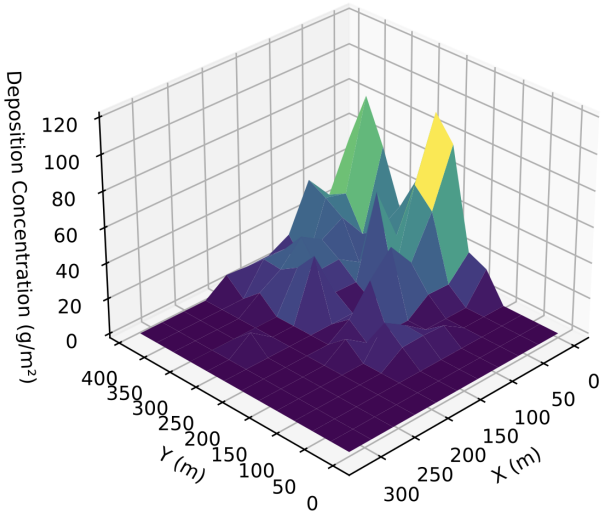

(b) STS-13.

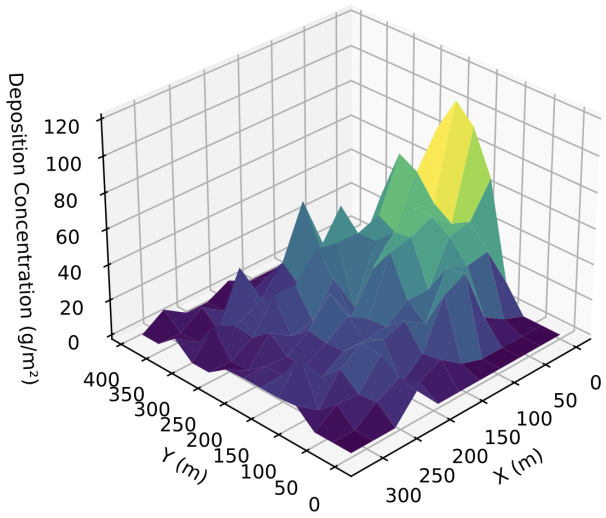

(c) STS-14.

Fig. 6 Predicted near-field acidic deposition concentration for STS-11, 13, and 14, where the positive x-axis points towards the north direction.

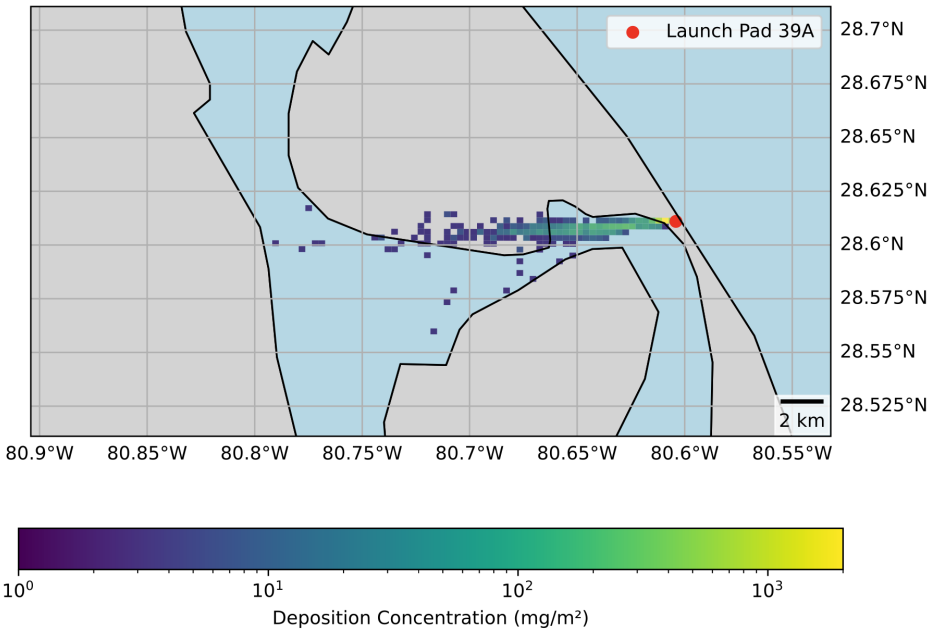

Fig. 7 Predicted far-field acidic deposition concentration for STS-51D.

mg/m^2, occur within approximately 5 km from the launch pad. Beyond the first kilometer, most part of the deposition concentration significantly decreases by two orders of magnitude.

Same analytical method was applied to STS-51B case. The B-1 site located just below the lower edge of the launch pad 39A (around 800 m under the northern edge of the launch pad). The observation shows the concentration of 4,246 and 5,303 mg/m^2. Figure 9 illustrates the predicted results for the STS-51D case, which has a maximum concentration of 2,420 mg/m^2. For the observed data, the B-3 site, which is located approximately 200 meters below the B-1 site, recorded concentrations of 923 mg/m^2 and 703 mg/m^2. Figure 10 indicates that only a specific area has a concentration exceeding 1,000 mg/m^2. Beyond that point, the concentration decreases significantly with increasing downwind distance.

The far-field deposition concentration validation indicates a good agreement between the predicted results and the observed data in terms of the order of magnitude of the deposition. However, the lack of observed data suitable for model validation, along with the scarcity of atmospheric data for the times and locations of certain Space Shuttle launches, poses a challenge in refining the model. Consequently, more comprehensive data collection is essential to improve the accuracy of future predictions.

D. Plume Prediction at Starbase, Boca Chica, Texas

The study extends to predict the plume evolution at Boca Chica, Texas, where Starbase is located. We selected three date times, consisting of April 20, 2023, at 13:00 UTC; November 18, 2023, at 13:00 UTC; and March 14, 2024, at 13:00 UTC, to follow SpaceX Starship's integrated flight tests 1, 2, and 3, respectively. We used the HRRR model to obtain meteorological data for each specific date and time. Although the spaceport configurations and launch vehicles vary, the model provides insights into plume evolution under the local atmospheric conditions. For the Starship, the choice of LOx/LCH4 as a propellant results in less harmful exhaust products for the environment and human health. However, nitric oxide (NO) can still be observed as one of the main products [34]. This compound can affect the respiratory system and may cause irritation to the skin and eyes.

In the near-field prediction, it can be observed from Table 6 that test 3 experienced strong winds at 12.22 m/s, surpassing those of STS-1 through STS-9. This resulted in a larger deposition area and a distance exceeding 1 km. Figure 11 shows the cumulative near-field deposition results. Table 7 shows far-field deposition results. As expected, strong wind can transport plume over 20 km from the launch pad. Figure 7 depict the far-field plume evolution for the mentioned cases. In the cases of test 1 and 3, the plumes are shown traveling northwest of the launch pad. Approximately 8.3 km north of the launch pad lies South Padre Island. Further to the northwest, Port Isabel is situated at a distance of 9 km from the launch site. Both South Padre Island and Port Isabel are residential areas, with Port Isabel having an

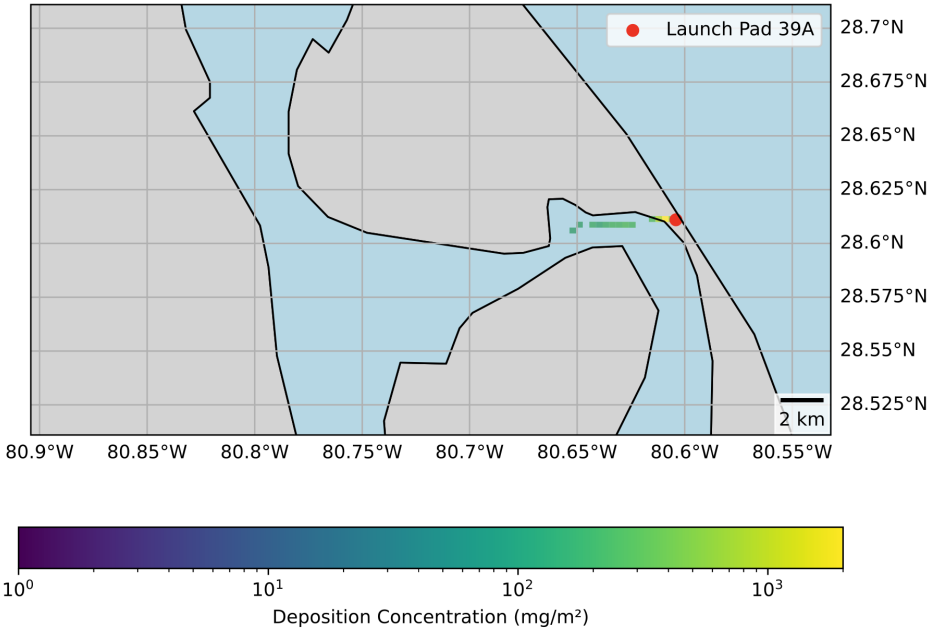

Fig. 8 Predicted far-field acidic deposition concentration for STS-51D, excluding deposition concentrations lower than 100 mg/m^2.

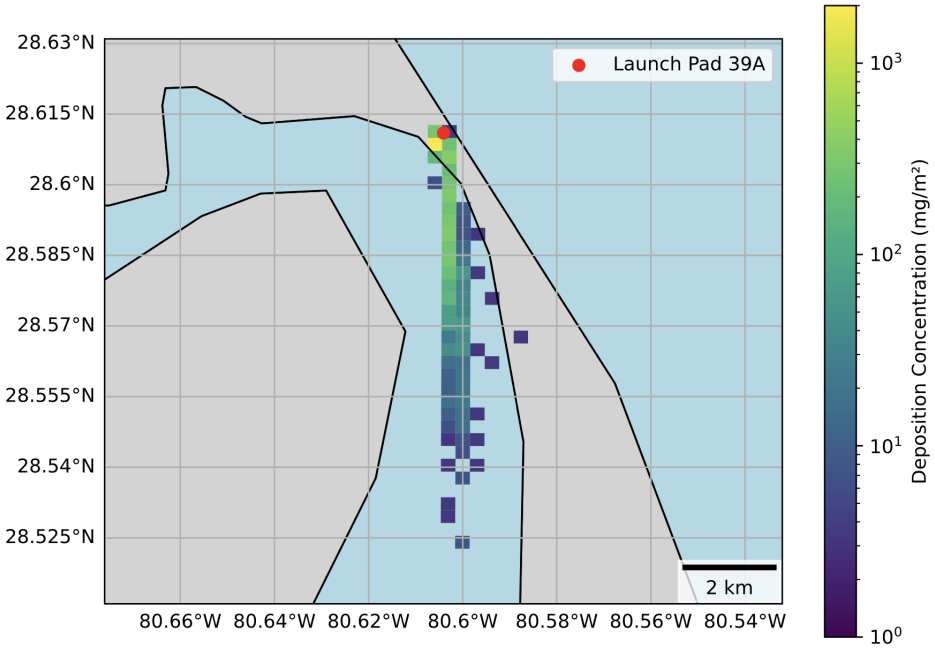

Fig. 9 Predicted far-field acidic deposition concentration for STS-51B.

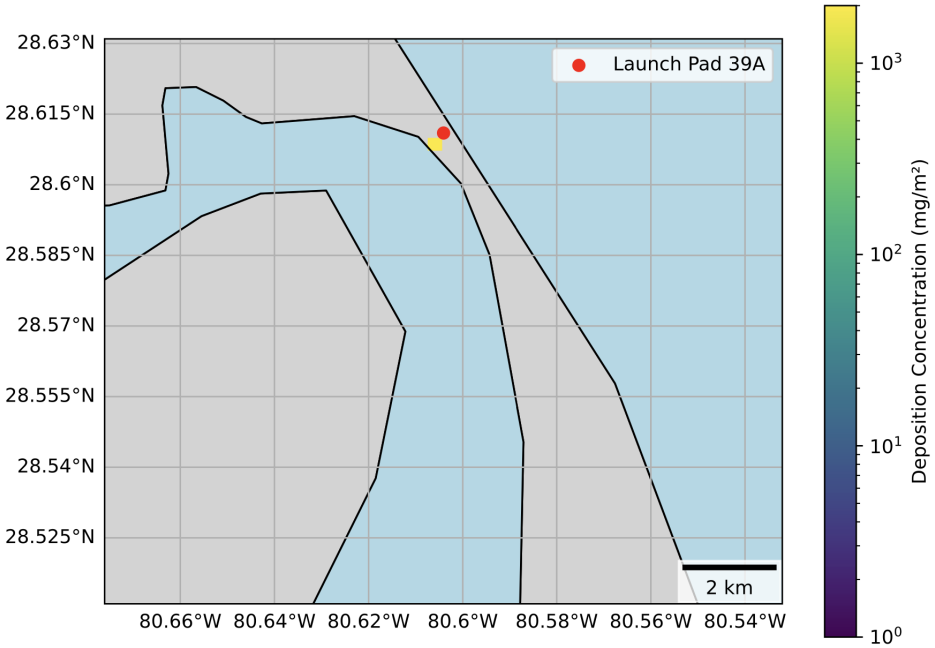

Fig. 10 Predicted far-field acidic deposition concentration for STS-51B, excluding deposition concentrations lower than 1,000 mg/m^2.

Table 6 Wind conditions and near-field launch deposition results for SpaceX Starship integrated flight test 1, 2, and 3.

Case	Wind speed (m/s)	Wind direction (deg. north)	Area (km^2)	Distance (m)
SpaceX Starship flight test-1	9.74	137	0.24	930
SpaceX Starship flight test-2	1.60	301	0.15	471
SpaceX Starship flight test-3	12.22	151	0.30	1,104

estimated population of around 6,000 in 2019 and South Padre Island having approximately 2,000 residents in 2022.

The study performed a statistical analysis of wind patterns to gain insights into each location. Understanding these wind statistics can inform the decision-making process regarding the selection and design of spaceport locations. In order to collect ground-level wind data at the Starbase launch pad, we randomly selected 100 date-time points throughout 2023, utilizing the HRRR model for our analysis. Figure 13 shows the occurences of the wind direction and magnitude at the SpaceX StarBase, Boca Chica, Texas and Launch pad 39A, Cape Canaveral, Florida. At the StarBase, the prevailing wind predominantly blows in a northwest direction 64% of the time. Additionally, 17% of wind observations point southwest, while winds blowing toward the northeast are comparatively rare, constituting only 4% of observations. Southeastern winds account for 15%. The figure also displays wind speeds in the radial direction of the graph, represented in m/s. The results indicate that the wind typically points in a northwest direction, encompassing areas such as Port Isabel and South Padre Island. Consequently, this prevailing wind direction is likely to carry the

Table 7 Far-field launch deposition results for SpaceX Starship integrated flight test 1, 2, and 3.

Case	Area (km^2)	Distance (km)
SpaceX Starship flight test-1	33.36	22.30
SpaceX Starship flight test-2	16.38	9.21
SpaceX Starship flight test-3	49.73	23.54

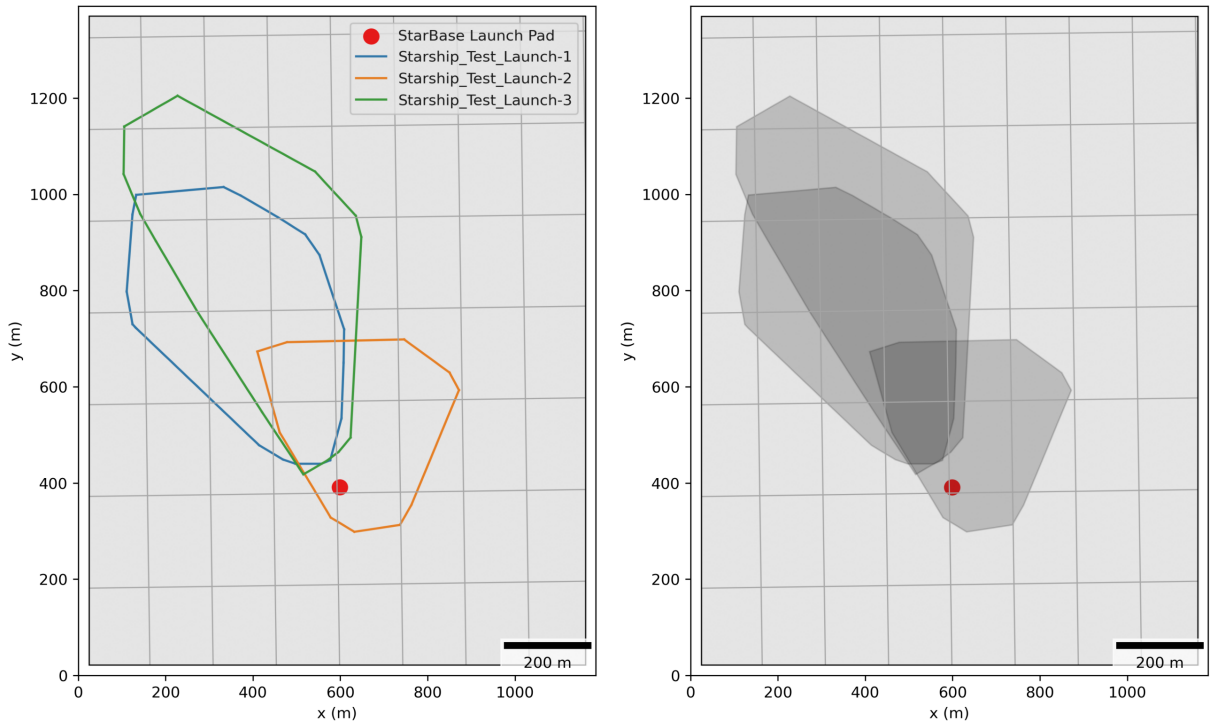

Fig. 11 Cumulative near-field launch deposition results for SpaceX Starship integrated flight test 1, 2, and 3.

rocket's plume towards the northwest as well. Compared with the wind statistics at Launch pad 39A, it can be seen a greater randomness in wind direction probability.

V. Discussion

The results indicate that the model has an ability to predict the acidic deposition resulting from the rocket exhaust plume. By incorporating the cloud rise model, it increases the adaptability of the model to accurately predict results under different meteorological conditions. The analysis at StarBase in Boca Chica, Texas, indicates that it is possible for the plume to reach residential areas, specifically Port Isabel and South Padre Island. The statistical analysis of wind data also reveals a strong likelihood of winds blowing in a northwest direction. It is useful to incorporate wind analysis into the main aspects of plume modeling.

The results align well with expectations, considering the limited data available for validation. Due to the lack of temporal and spatial wind data beyond the 39A launch pad at KSC, we have had to assume constant wind conditions over time and across different locations. This assumption particularly affects the accuracy of the far-field deposition model, as the plume may travel for up to 30 minutes and cover distances up to 22 km from the launch pad [5]. However, a positive aspect is the comprehensive altitude data available for each launch, which is provided at intervals of every 100 ft, offering valuable insight into dispersion patterns across altitude. Using the HRRR model to simulate recent launches provides more comprehensive atmospheric data across time and locations. However, the HRRR model only offers four usable layers at altitudes of 0, 761.7, 1456.7, and 3010.9 m. The lack of validation data prevents comprehensive verification of far-field deposition concentration predictions, which affects the validity of the far-field deposition model.

The results contribute to a clearer understanding of a rocket's ground cloud evolution. The Rocket Exhaust Effluent Diffusion Model (REEDM) has been widely used to predict the deposition from rocket ground clouds. The study by Eckman in 1996 [35] was used to conduct comparisons between the model from this study and REEDM. Our study incorporates a more comprehensive method to utilize atmospheric data. This improved model accounts for the complex dynamics of plume dispersion, including the variability of wind speeds and directions at different altitudes. REEDM employs bulk parameters derived from a large vertical averaging of wind speed and direction to inform the model's

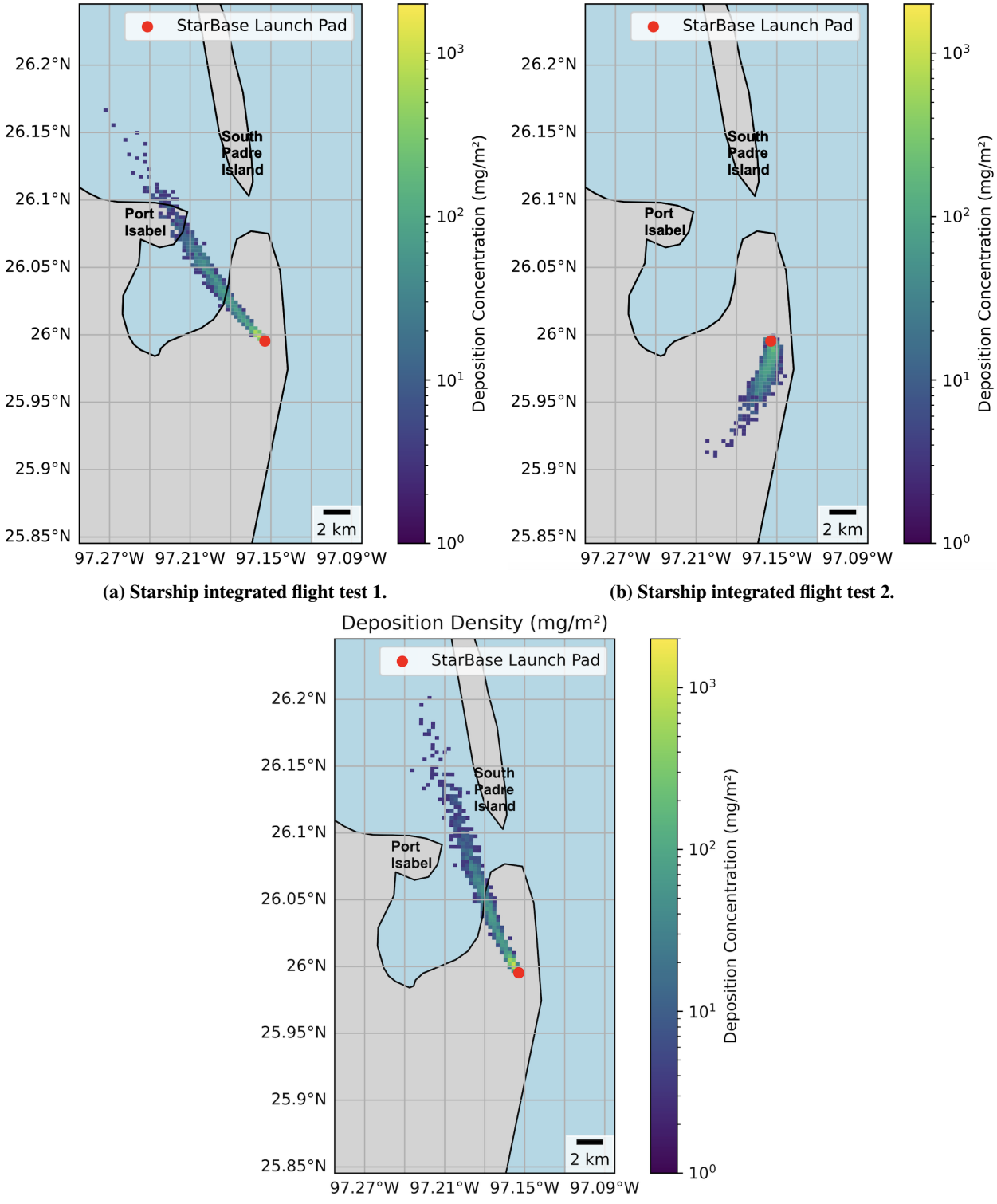

(a) Starship integrated flight test 1.

(b) Starship integrated flight test 2.

(c) Starship integrated flight test 3.

Fig. 12 Far-field launch deposition results for SpaceX Starship integrated flight test 1, 2, and 3.

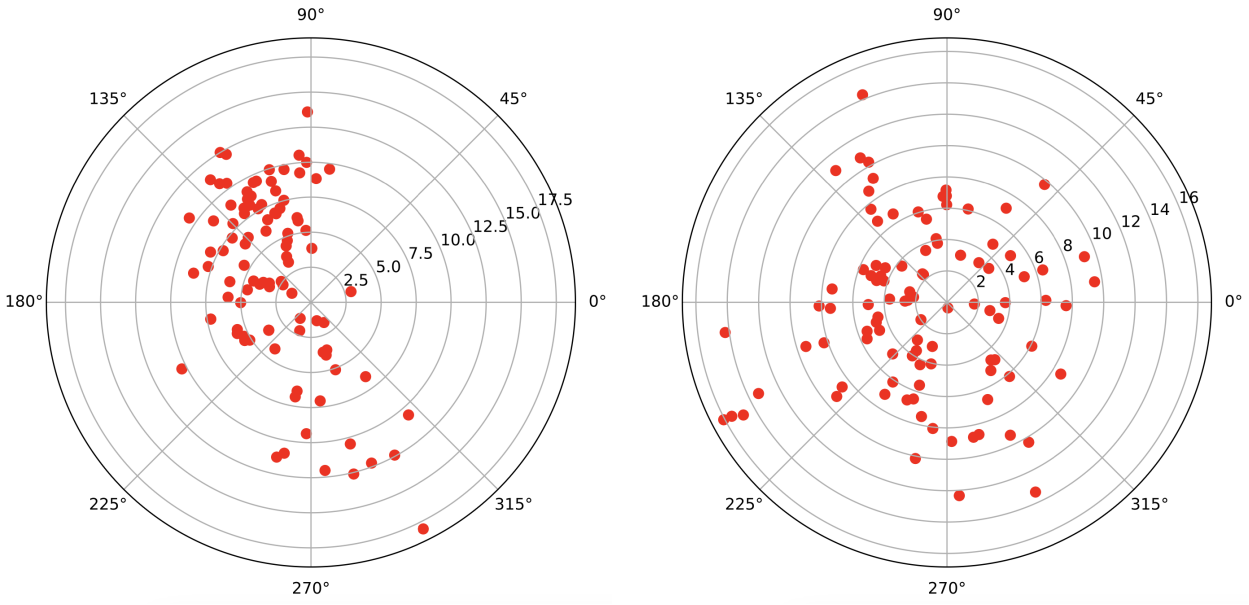

(a) SpaceX StarBase, Boca Chica, Texas. **(b) Launch pad 39A, Cape Canaveral, Florida.**

Fig. 13 Wind direction and magnitude distribution at SpaceX StarBase and launch pad 39A in 2023, where 90°points towards north direction.

dynamics, rather than allowing atmospheric conditions to vary with altitude. A critical shortcoming of REEDM is its lack of prediction capability within the near-field zone, which can have heavy deposition. In practice, measured concentrations of materials such as chlorides and aluminum near the launch site have been found to significantly exceed REEDM's predictions [7]. Moreover, the maximum danger zone affected by near-field deposition was measured at 1.41 km for launch pad 39A and 1.98 km for launch pad 39B, respectively [5]. These findings highlight the need for spaceport design considerations that address the risk of hazardous acidic deposition that could extending into the operating areas. Our model addresses this gap by configuring specific setups for near-field deposition, leading to quantitatively more accurate predictions of concentration, area, and distance for deposition.

Future studies should account for the comprehensive composition of the ground cloud. Understanding the behavior of each substance is key to assessing its impact on air quality, a critical concern for human health that is governed by stringent regulations. Additionally, the study of atmospheric turbulence modeling might enhance the accuracy of models, leading to a more realistic representation of real-world atmospheric conditions. Furthermore, this model can serve as one of the modules to determine the optimal spaceport location. Several aspects need to be considered when evaluating potential spaceport sites. The Spaceport Facility Location Planning Model (SFLP) aims to optimize the spaceport location while minimizing costs, taking into account transportation costs, operational costs, mission launch costs, and flight rerouting costs. A preliminary output scenario from the SFLP identifies the following locations in the US as potential locations for future spaceports: Humboldt, CA; Matagorda, TX; Gulf, FL; Dare, NC; Monroe, FL; and Washington, ME [36]. These results provide a strong foundation for narrowing down the future implementation of the plume evolution model at the specific locations to assess environmental impact. Wind statistics at each potential site could serve as a valuable starting point for a preliminary analysis.

VI. Conclusion

This research developed a rocket plume evolution model with the goal of predicting acidic deposition resulting from the transport of the launch ground cloud. A LPDM, integrated with a distinct cloud rise model to drive the buoyancy mechanism, was utilized. Model validation was conducted in three aspects: the dynamics of cloud rise, the characteristics of acidic deposition and the concentration of acidic deposition. This study employed the "2/3 law" to predict the cloud rise, coupled with the cloud properties derived from the ideal gas law. The cloud rise model demonstrated good agreement after model fitting was conducted, which resulted in an initial vertical velocity of the

cloud of 3.50 m/s. However, the STS-3 presented challenges to the cloud rise model, indicated by a negative R-squared value and a high RMSE, whereas other cases showed R-squared values above 0.80 and RMSEs lower than 125.0 m. This presents uncertainties associated with atmospheric modeling.

Near-field deposition resulting from the exhaust of initial blasts of the SRBs. The characteristics of near-field deposition were validated by comparing with cumulative near-field deposition data observed for STS-1 through STS-9 [7, 13]. The results demonstrate a good agreement with the observed data in terms of deposition patterns. Furthermore, The deposition distance are reasonable and acceptable when compared with the observed measurements. The deposition area ranged from 0.11 to 0.20 km^2, and the farthest distance from the launch pad was found to range from 428 to 744 m. The deposition concentration aspect was validated by comparing with the STS-11, 13, and 14 launch cases, which provided 3-D deposition concentration graphs. Results show a good preliminary alignment with expected patterns, yet they underscore the necessity for further comprehensive studies to increase confidence in the findings.

Far-field deposition model was incorporated with the cloud rise model, expanding its adaptability to predict the deposition under various atmospheric conditions. Far-field deposition results from the fallout of acidic mixtures released from the ground cloud as it ascends and stabilizes. We implemented models for five STS cases - 1, 2, 5, 6, and 7. The characteristics of far-field deposition demonstrate the model's ability to capture significant deposition patterns. Nevertheless, accurately predicting the extent and range of the deposition area poses considerable challenges. Moreover, the method used to obtain observation data, using copper plates, made it challenging to measure a comprehensive deposition [8]. STS-51D and STS-51B are the two launch cases that provided useful deposition concentration data at each study site for far-field analysis. These cases were utilized to validate the far-field deposition model with respect to concentration. Due to the limited data available, only three sites for STS-51D and two for STS-51B were used in validation. The validation of the model was conducted by comparing the order of magnitude of the deposition concentrations, with which the model showed good agreement.

This study expanded the simulation to include near-field and far-field deposition for the SpaceX Starship integrated flight tests 1, 2, and 3. The results show the strong potential for far-field deposition to reach residential areas such as Port Isabel and South Padre Island, which are located north and northwest of the launch pad, respectively. Analysis of the wind data at the launch pad indicates that the wind is more likely to point westward (81%), with 79% of that likelihood accounting for the northwest direction. In contrast to launch pad 39A at Cape Canaveral, where wind patterns show even distribution in all directions. Wind statistics would be helpful for a primary analysis of the environmental impact of rocket plumes.

The predictive simulations of far-field deposition from the STS-51D and STS-51B shuttle launches at KSC, alongside the StarShip launches at StarBase, indicate that chloride concentrations could exceed 1,000 mg/m^2. It is important to emphasize that these findings are preliminary and are based on simulations rather than final results. This amount of concentration could potentially give a considerable damage to various species [8]. However, these concentrations were observed within 1 km of the launch pad, underscoring the finding that there was minimal impact on far-field deposition, with no observed plant mortality or changes in the structure of plant communities [12].

Acknowledgments

This work was supported by funding from the University of Michigan College of Engineering through the Seeding To Accelerate Research Themes (START) program.

References

[1] Dallas, J., Raval, S., Gaitan, J. A., Saydam, S., and Dempster, A., "The environmental impact of emissions from space launches: A comprehensive review," *Journal of Cleaner Production*, Vol. 255, 2020, p. 120209. https://doi.org/10.1016/j.jclepro.2020.120209.

[2] Hall, C. R., Schmalzer, P. A., Breininger, D. R., Duncan, B. W., Drese, J. H., Scheidt, D. A., Lowers, R. H., Reyier, E. A., Holloway-Adkins, K. G., Oddy, D. M., et al., "Ecological impacts of the space Shuttle Program at John F. Kennedy Space Center, Florida," Tech. Rep. TM-2014–216639, National Aeronautics and Space Administration, 2014.

[3] Dreschel, T. W. and Hall, C. R., "Quantification of hydrochloric acid and particulate deposition resulting from space shuttle launches at John F. Kennedy space center, Florida, USA," *Environmental Management*, Vol. 14, 1990, pp. 501–507.

[4] Potter, A., "Space Shuttle Environmental Effects: The First 5 Flights," Tech. Rep. NASA-CR-171812, Houston, TX, USA, 1983.

[5] Duncan, B. W. and Schmalzer, P. A., "Using a geographical information system for monitoring space shuttle launches: determining cumulative distribution of deposition and an empirical test of a spatial model," *Environmental Management*, Vol. 18, No. 3, 1994, pp. 465–474. https://doi.org/10.1007/BF02393874.

[6] Hwang, B. and Gould, R. K., "Rocket exhaust ground cloud/atmospheric interactions," Tech. Rep. NASA-CR-2978, National Aeronautics and Space Administration, 1978.

[7] SCHMALZER, P., HALL, C., Hinkle, C., DUNCAN, B., KNOTT, W., III, and SUMMERFIELD, B., "Environmental monitoring of space shuttle launches at Kennedy Space Center-The first ten years," *31st Aerospace Sciences Meeting*, 1992, p. 303.

[8] Schmalzer, P. A., Hinkle, C. R., and Dreschel, T. W., "Far-Field Deposition from Space Shuttle Launches at John F. Kennedy Space Center, Florida," Tech. Rep. NASA Technical Memorandum 83104, The Bionetics Corporation, Kennedy Space Center, Florida, 1986.

[9] Turner, R. E., "MSFC exhaust effluent diffusion predictions and measurements for STS-1, STS-2, STS-3, and STS-4," Tech. rep., 1983.

[10] Gregory, G. L., Woods, D. C., and Sebacher, D. I., "Airborne measurements of launch vehicle effluent: Launch of Space Shuttle (STS-1) on 12 April 1981," Tech. rep., 1983.

[11] Bjorklund, J., Dumbauld, R., Cheney, C., and Geary, H., "User's manual for the REEDM (Rocket Exhaust Effluent Diffusion Model) computer program," Tech. Rep. NASA-CR-3646, NASA, 1982.

[12] NASA, "Final environmental impact statement for the Mars 2020 mission," 2014.

[13] Schmalzer, P., Hinkle, C., and Breininger, D., "Effects Of Space Shuttle Launches STS-1 Through STS-9 On Terrestrial Vegetation Of John F. Kennedy Space Center, Florida," *Kennedy Space Center, Florida. NASA TM*, Vol. 83103, 1985, p. 39.

[14] Lo, C., Bons, J., Yao, Y., and Capecelatro, J., "Assessment of stochastic models for predicting particle transport and deposition in turbulent pipe flows," *Journal of Aerosol Science*, Vol. 162, 2022, p. 105954.

[15] Briggs, G. A., "Plume rise predictions," *Lectures on air pollution and environmental impact analyses*, Springer, 1975, pp. 59–111.

[16] Tanaka, H. L. and Iguchi, M., "Numerical simulations of volcanic ash plume dispersal for Sakura-Jima using real-time emission rate estimation," *Journal of Disaster Research*, Vol. 14, No. 1, 2019, pp. 160–172. https://doi.org/10.20965/jdr.2019.p0160.

[17] Searcy, C., Dean, K., and Stringer, W., "PUFF: A high-resolution volcanic ash tracking model," *Journal of Volcanology and Geothermal Research*, Vol. 80, No. 1-2, 1997, pp. 1–16. https://doi.org/10.1016/S0377-0273(97)00037-1.

[18] Sand, P. F., "An investigation of instantaneous plume rise from rocket exhaust," 1996.

[19] Anfossi, D., "Analysis of plume rise data from five TVA steam plants," *Journal of Applied Meteorology and Climatology*, Vol. 24, No. 11, 1985, pp. 1225–1236.

[20] Anfossi, D., Ferrero, E., Brusasca, G., Marzorati, A., and Tinarelli, G., "A simple way of computing buoyant plume rise in Lagrangian stochastic dispersion models," *Atmospheric Environment. Part A. General Topics*, Vol. 27, No. 9, 1993, pp. 1443–1451.

[21] Hart, W., "Dynamics of large buoyant clouds generated by rocket launches," 1972.

[22] Backlund, S. and Rossen, J., "A study of performance and cost improvement potential of the 120 inch (3.05 m) diameter solid rocket motor. Volume 2: Study approach and detailed results," Tech. rep., 1971.

[23] NASA, "STUDY OF SOLID ROCKET MOTORS FOR A SPACE SHUTTLE BOOSTER FINAL REPORT," Tech. Rep. NASA-CR-123623, National Aeronautics and Space Administration, 1972.

[24] Anderson, B. J. and Keller, V. W., "Space Shuttle Exhaust Cloud Properties," Tech. Rep. NASA Technical Paper 2258, National Aeronautics and Space Administration, 1983.

[25] Susko, M. and Kaufman, J. W., "Exhaust cloud rise and growth for Apollo Saturn engines." *Journal of Spacecraft and Rockets*, Vol. 10, No. 5, 1973, pp. 341–345.

[26] Susko, M., Kaufman, J. W., and Hill, K., "Rise Rate and Growth of Static Test Vehicle Engine Exhaust Clouds," *TM X-53782, Aero-Astrodynamics Research Review*, , No. 7, 1968, pp. 146–166.

[27] Stephens, J. B., Susko, M., Kaufman, J. W., and Hill, C. K., "An analytical analysis of the dispersion predictions for effluents from the Saturn 5 and Scout-Algol 3 rocket exhausts," Tech. rep., 1973.

[28] Gregory, G. L., Hulten, W. C., and Wornom, D. E., "Apollo Saturn 511 effluent measurements from the Apollo 16 launch operations: An experiment," Tech. rep., 1974.

[29] Johnson, D. L., Jasper, G., and Brown, S. C., "Atmospheric Environment for Space Shuttle (STS-1) Launch," Tech. Rep. NASA-TM-82436, National Aeronautics and Space Administration, 1981.

[30] Johnson, D. L. and Brown, S. C., "Atmospheric Environment for Space Shuttle (STS-2) Launch," Tech. Rep. NASA-TM-82463, National Aeronautics and Space Administration, 1981.

[31] Johnson, D. L., Hill, C. K., and Batts, G. W., "Atmospheric Environment for Space Shuttle (STS-5) Launch," Tech. Rep. NASA-TM-82515, National Aeronautics and Space Administration, 1983.

[32] Johnson, D. L., Hill, C. K., and Batts, G. W., "Atmospheric Environment for Space Shuttle (STS-6) Launch," Tech. Rep. NASA-TM-82529, National Aeronautics and Space Administration, 1983.

[33] Johnson, D. L., Hill, C. K., and Batts, G. W., "Atmospheric Environment for Space Shuttle (STS-7) Launch," Tech. Rep. NASA-TM-82542, National Aeronautics and Space Administration, 1983.

[34] Sirieys, E., Gentgen, C., Jain, A., Milton, J., and de Weck, O., "Space sustainability isn't just about space debris: On the atmospheric impact of space launches," *MIT Science Policy Review*, Vol. 3, 2022, pp. 143–151.

[35] Eckman, R. M., Nappo, C. J., and Rao, K. S., "Rocket exhaust effluent diffusion model (REEDM) verification and sensitivity study," 1996.

[36] Wu, H., Sun, K. R., Miller, J. A., Jia-Richards, O., and Li, M. Z., "Spaceport Facility Location Planning within the US National Airspace System," *arXiv preprint arXiv:2402.11389*, 2024.